

Distinguishing the Observational Signatures of Hot Spots Orbiting Reissner-Nordström Spacetime

Tianshu Wu^{*} and Yiqian Chen[†]

*Center for Theoretical Physics, College of Physics,
Sichuan University, Chengdu, 610064, China*

This paper delves into observable signatures of hot spots orbiting Reissner-Nordström (RN) black holes and naked singularities. In a RN black hole case, we find two discernible lensing image tracks in time integrated images capturing a complete orbit of hot spots, and a image shadow within the critical curve where photons with a small impact parameter fall into the event horizon. Conversely, in RN singularities, additional image tracks can be found inner the critical curve, originating from photons reflected by the infinitely high effective potential well. Moreover, we found incomplete and converge tracks from the time integrated images of hot spot orbiting RN singularities lacking of a photon sphere. The presence of these additional image tracks exerts a significant influence on temporal magnitudes at their local maxima, allowing us to differentiate between RN black holes and RN naked singularities.

arXiv:2402.06413v1 [gr-qc] 9 Feb 2024

^{*} wutianshu@stu.scu.edu.cn

[†] yqchen@stu.scu.edu.cn

CONTENTS

I. Introduction	2
II. Set up	3
III. Celestial Sphere Model	6
IV. Hot Spot Model	7
A. Integrated Images	9
B. Temporal Fluxes and Centroids	11
V. Conclusions	15
Acknowledgments	16
References	16

I. INTRODUCTION

Recent advancements in gravitational physics have been propelled by a surge in high-precision experiments, notably spearheaded by collaborations like the Event Horizon Telescope (EHT). They have yielded groundbreaking discoveries, including the detection of shadow-like features near supermassive black holes [1–14]. These experimental triumphs align closely with theoretical predictions, notably supporting the Kerr hypothesis [15], which posits that the endpoint of gravitational collapse in suitable astrophysical conditions results in the formation of rotating, electrically neutral black holes [16, 17]. This convergence of theory and observation not only validates our understanding of black hole physics but also opens avenues for exploring unresolved questions in the realm of strong gravitational fields. Furthermore, physicists continue to refine simplified models to numerically explore black hole properties, including accretion disks and celestial spheres, enhancing our understanding of these enigmatic cosmic entities.

A defining feature of images captured by the EHT is a dark, central region surrounded by a bright ring. This feature emerges from the bending of light due to strong gravity near unstable photon orbits [18–25]. These observations align well with the Kerr black hole model. However, the discovery of photon spheres around exotic compact objects (ECOs) has introduced complexities [26–35]. ECOs mimic black hole observations but predict unique signatures for further verification.

Therefore, their observation becomes a scientific target for the next-generation Event Horizon Telescope (ngEHT) [36].

Naked singularities, a type of ECO, have garnered significant interest. Despite the cosmic censorship conjecture forbidding naked singularities, they can theoretically form under specific conditions during the collapse of massive objects [37–43]. With photon spheres, naked singularities can closely resemble black holes optically, prompting investigations into their unique observational signatures [44–55]. Notably, research indicates that naked singularities in Reissner-Nordström (RN) geometries possess an anti-photon sphere, reversing the inner image that does not match the observed shadow [48]. Therefore, investigating the distinct observational characteristics of RN naked singularities and RN black holes holds significant value.

On the other hand, several general relativistic magnetohydrodynamics (GRMHD) simulations and semi-analytic models suggest that the interplay of magnetic reconnection and flux eruptions can lead to the formation of hot spots around supermassive black holes residing within magnetized accretion disks [56–58]. Interestingly, these hot spots have been repeatedly observed in the vicinity of Sgr A* [59–61]. Moreover, an intriguing instance involved the detection of an orbiting hot spot in unresolved light curve data at the EHT observing frequency [62]. Due to their origin from a compact region very close to the innermost stable circular orbit (ISCO), these hot spots offer a promising avenue for probing central objects in the strong gravity regime [63–68]. This work focuses on investigating the distinctive signatures of hot spots around different RN singularities and RN black holes to potentially distinguish them.

The subsequent sections of this paper are structured as follows: In Section II, we briefly introduce RN spacetime, along with a discussion of geodesic motion within these spacetimes. In Section III, we show the numerical results of the celestial model in RN spacetime. Section IV is devoted to the hot spot model, followed by an examination time integrated images, temporal magnitudes and centroids. Finally, Section V presents our conclusions. We adopt the convention $G = c = 1$ throughout the paper.

II. SET UP

This section commences with a concise overview of geodesic expressions within RN spacetime. To enhance the significance of the chosen orbit in our hot spot model, we also provide a brief introduction to diverse stable circular orbits within the framework of RN spacetime.

The RN metric presents a static solution in Einstein and Maxwell equations, which is given by

$$ds^2 = -f(r) dt^2 + \frac{1}{f(r)} dr^2 + r^2 (d\theta^2 + \sin^2 \theta d\varphi^2), \quad (1)$$

with the metric function

$$f(r) = 1 - \frac{2M}{r} + \frac{Q^2}{r^2}. \quad (2)$$

Here, M and Q represent the mass and the electric charge, respectively. Conditions $M < Q$ and $M > Q$ correspond to the two scenarios of naked singularities and black holes, respectively. The trajectory of a test particle with four-momentum p^μ is determined by the geodesic equations

$$\frac{dx^\mu}{d\lambda} = p^\mu, \quad \frac{dp^\mu}{d\lambda} = -\Gamma_{\rho\sigma}^\mu p^\rho p^\sigma, \quad (3)$$

where λ is the affine parameter, and $\Gamma_{\rho\sigma}^\mu$ indicates the Christoffel symbol. These geodesics are fully characterized by three conserved quantities,

$$E = -p_t, \quad L_z = p_\varphi, \quad L^2 = p_\theta^2 + L_z^2 \csc^2 \theta. \quad (4)$$

In the context of massless particles, the conserved quantities E , L_z and L represent the total energy, the angular momentum parallel to the axis of symmetry and the total angular momentum, respectively. Additionally, the Hamiltonian constraint $\mathcal{H} \equiv g_{\mu\nu} p^\mu p^\nu / 2 = 0$ yields the radial component of the null geodesic equations as

$$\dot{r}^2 + V_{\text{eff}}(r) = 0, \quad (5)$$

where the dot signifies differentiation with respect to an affine parameter λ , and the introduced effective potential is given by

$$V_{\text{eff}}(r) = f(r) \left[\frac{L^2}{r^2} - \frac{E^2}{f(r)} \right]. \quad (6)$$

A circular null geodesic occurs at an extremum of the effective potential $V_{\text{eff}}(r)$, and the radius r_c of this geodesic is determined by the conditions

$$V_{\text{eff}}(r_c) = 0, \quad V'_{\text{eff}}(r_c) = 0. \quad (7)$$

Furthermore, local maxima and minima of the effective potential correspond to unstable and stable circular null geodesics, which constitute the photon sphere and the anti-photon sphere, respectively. When $Q/M \leq \sqrt{9/8}$, a photon sphere exists at $r = r_{ps}^+$, and an anti-photon sphere exists at $r = r_{ps}^-$, as given by

$$r_{ps}^\pm = \frac{3M \pm \sqrt{9M^2 - 8Q^2}}{2}. \quad (8)$$

Q/M Value	Region of stable circular orbit	Photon Sphere
$Q/M < 1$	$r > r_{\text{msco}}$	Existent
$1 < Q/M < \sqrt{9/8}$	$r_* < r < r_{ps}^-$ and $r > r_{\text{msco}}^+$	
$\sqrt{9/8} < Q/M < \sqrt{5}/2$	$r_* < r < r_{\text{msco}}^-$ and $r > r_{\text{msco}}^+$	Non-Existent
$Q/M > \sqrt{5}/2$	$r > r_*$	

TABLE I. Region of stable circular orbit and photon sphere. The analytical expressions for r_{msco} and r_{msco}^\pm are given in [69].

For massive particles, E , L_z and L represent the total energy per unit mass, the angular momentum per unit mass parallel to the axis of symmetry and the total angular momentum per unit mass, respectively, when the affine parameter λ is chosen as the proper time per unit mass. Similarly, the Hamiltonian constraint $\mathcal{H} = -1/2$ leads to the effective potential

$$V_{\text{eff}}(r) = f(r) \left[\frac{L^2}{r^2} - \frac{E^2}{f(r)} + 1 \right]. \quad (9)$$

and circular time-like geodesics satisfy

$$V_{\text{eff}}(r) = 0, V'_{\text{eff}}(r) = 0. \quad (10)$$

A comprehensive analysis of the circular motion of time-like particles have been studied in [69, 70]. In the presence of a photon sphere ($Q/M \leq \sqrt{9/8}$) and ensuring the motion of the particle satisfies $E > 0$ and $L > 0$, it is evident that circular time-like geodesics exist only when $r > r_{ps}^+$, $r < r_{ps}^-$ and $r > r_* = Q^2/M$. In contrast, as photon spheres do not exist ($Q/M > \sqrt{9/8}$), circular time-like geodesics exist when $r > r_*$. Besides, the existence of stable circular orbits is also bounded by the Marginal Stable Circular Orbits (MSCOs) with the additional condition

$$V''_{\text{eff}}(r) = 0. \quad (11)$$

This condition (11) yields a single solution r_{msco} , two solutions r_{msco}^\pm and no solution for a RN black hole with $Q/M < 1$, a RN naked singularity with $1 < Q/M < \sqrt{5}/2$ and a RN naked singularity with $Q/M > \sqrt{5}/2$, respectively. Combining these findings with the results derived from eqns. (10) regarding the existence of circular orbits, we collate four parameter spaces with distinct regions of stable circular orbits, as outlined in the Table. I.

In the numerical simulation presented below, our primary focus lies in comparing the simulation results for $Q/M = 0.9, 1.05$ and 1.11 . These specific values are chosen to represent distinct scenarios, namely, black holes, naked singularities with a photon sphere, and naked singularities without a photon sphere, respectively.

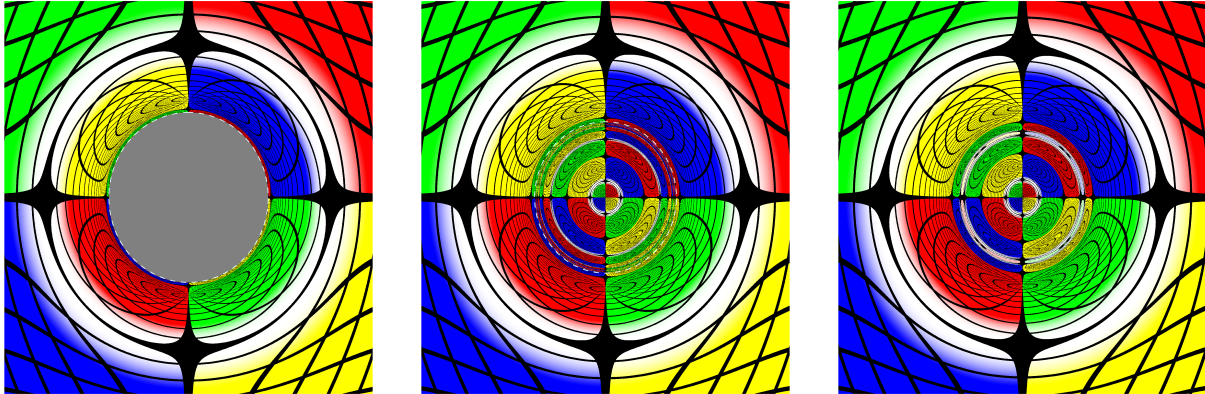


FIG. 1. Images of a celestial sphere located at $r = 25M$ in the RN metric with $Q/M = 0.9$ (**Left**), 1.05 (**Middle**) and 1.1 (**Right**). The observer's location is $x_{\text{o}}^{\mu} = (0, 10M, \pi/2, \pi)$, and the field of view spans $2\pi/5$. Dashed lines represent the critical curve, formed by light rays emitted from the photon sphere. The left panel exhibits one Einstein ring, while the middle and right panels display three Einstein rings. In the case of $Q/M = 0.9$, corresponding to a black hole, the image encompasses the black hole shadow portrayed as a gray area in the left panel. The middle panel illustrates the image of a naked singularity with a photon sphere, where the region outside the critical curve shows little deviation from the left panel. However, within the critical curve, additional celestial images are also present. Moreover, near the critical curve, there exist infinitely high-order images. For the right panel, lacking a critical curve due to the absence of a photon sphere, the overall pattern is similar to the middle panel. Nevertheless, finite high-order images are observed near the second Einstein ring.

III. CELESTIAL SPHERE MODEL

This section utilizes numerical simulation to visualize gravitational lensing around RN spacetime for an intuitive understanding of light propagation. We model a celestial sphere source, divided into four color-coded quadrants, with a white dot placed in front of the observer. Additionally, a grid of black lines, spaced at $\pi/18$ intervals, overlays the image to indicate constant longitude and latitude. To generate observational images, we vary the observer's viewing angle and numerically integrate 2000×2000 photon trajectories until they intersect with the celestial sphere. For a detailed explanation of the numerical implementation, interested readers can refer to [55].

FIG. 1 depicts images of the celestial sphere in both RN black holes and singularities. Dashed circular lines depicted the critical curves, shaped by light rays escaping the photon spheres. The left panel displays the celestial sphere image for $Q/M = 0.9$. It includes the black hole shadow rendered in gray, an Einstein ring, and some higher-order images visible outside the critical curve.

The middle panel of FIG. 1 depicts the celestial sphere image for a RN naked singularity of

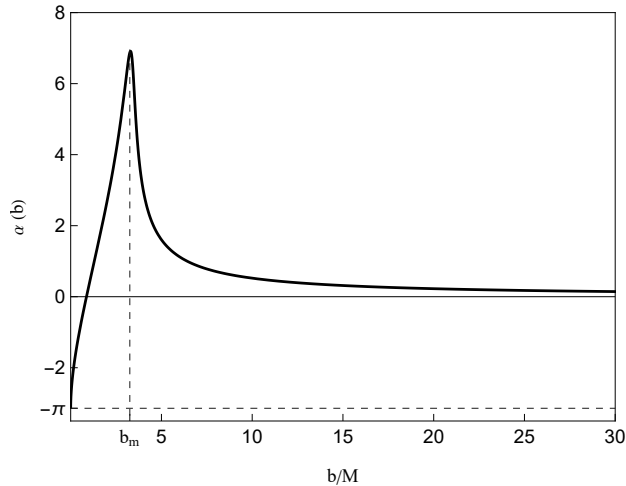


FIG. 2. The deflection angle $\alpha(b)$ as a function of the impact parameter b for $Q/M = 1.1$. The deflection angle reaches its maximum at $b = b_m$.

$Q/M = 1.05$, possessing a photon sphere. Similar to the $Q/M = 0.9$ case, the region outside the critical curve shows a comparable appearance. However, light ray refraction within the photon sphere leads to additional celestial images appearing inside the critical curve. Furthermore, compression and color alternation near the critical curve indicate the generation of numerous higher-order terms in its vicinity.

The right panel of FIG. 1 displays the celestial sphere image for a RN naked singularity of $Q/M = 1.1$, devoid of photon spheres. This image resembles the middle panel at a distance from the critical curve. However, the infinitely higher-order images converging near the critical curve are replaced by a finite number of higher-order images.

To understanding the finite number of higher-order images in the case of $Q/M = 1.1$, we analyze the deflection angle as a function of the impact parameter b , depicted FIG. 2. In this figure, the deflection angle is defined as $\alpha(b) = I(b) - \pi$, where the $I(b)$ is numerically integrated (details in [55, 71]). Notably, as the impact parameter b varies from 0 to the infinity, the deflection angle exhibits a maximum at b_m , leading to the absence of infinitely higher-order images.

IV. HOT SPOT MODEL

This section addresses the observational characteristics exhibited by hot spots surrounding RN black holes and naked singularities. Consistent with available data and theoretical analyses, flares likely originate from synchrotron radiation emitted by matter near the innermost stable circular orbit (ISCO) [63, 72, 73]. To accurately predict flare properties, we maintain hot spot orbits close

to the ISCO. For the RN black hole with $Q/M = 0.9$, a single stable orbit region exists, so the MSCO with radius r_{msco} is chosen. Conversely, RN naked singularities with $Q/M = 1.05$ and 1.1 exhibit two distinct stable orbit regions (discussed in Sec. II). We investigate hot spots in both outer and inner regions. In the outer region, the outer MSCO with radius r_{msco}^+ is adopted as the orbit of the hot spot. In the inner region, an orbit near radius r^* is chosen, as $r = r^*$ implies a geodesic with zero angular momentum. Specifically, for $Q/M = 1.05$ and 1.1 , inner orbits at $r = 1.11M$ and $1.22M$, respectively, are designated for the hot spots.

To simplify calculations, we model the hot spot as an isotropically emitting sphere and utilize our computational framework described in [63, 65, 66, 74]. Within this framework, the observer is positioned at $(t_o, r_o, \theta_o, \varphi_o) = (t_o, 100M, \theta_o, \pi)$. For computational efficiency and precision, we use a 1000×1000 pixel grid for each snapshot and generate 500 snapshots for a period of the orbit, ensuring smooth image evolution throughout period T_e . At a specific time t_k , each pixel in the image plane receives an intensity I_{klm} , collectively forming lensed hot spot images. We then analyze the following image properties, following [65, 66],

- Time integrated image:

$$\langle I \rangle_{lm} = \sum_k I_{klm}. \quad (12)$$

- Total temporal flux:

$$F_k = \sum_l \sum_m \Delta\Omega I_{klm}, \quad (13)$$

where $\Delta\Omega$ corresponds to the solid angle of a pixel.

- Temporal magnitude:

$$m_k = -2.5 \lg \left(\frac{F_k}{\min(F_k)} \right). \quad (14)$$

- Temporal centroid:

$$\vec{c}_k = F_k^{-1} \sum_l \sum_m \Delta\Omega I_{klm} \vec{r}_{lm}, \quad (15)$$

where \vec{r}_{lm} represents the position relative to the image center.

A. Integrated Images

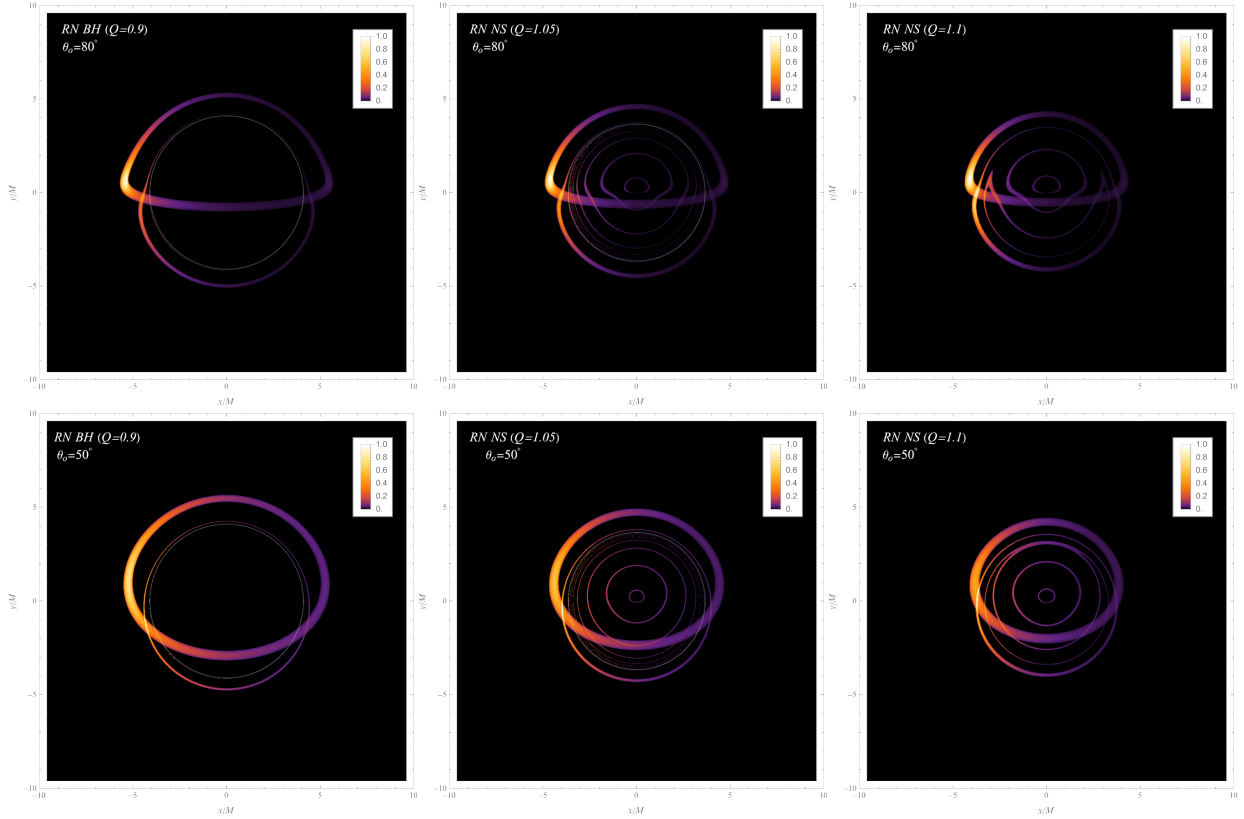


FIG. 3. Time integrated images depicting a full orbit of the hot spot are obtained from an observational inclination angle of $\theta_o = 80^\circ$ (**Upper Row**) and $\theta_o = 50^\circ$ (**Lower Row**). Note that the intensity are normalized with respect to their maximum value. The white lines delineate the critical curves, shaped by light rays escaping from the photon spheres. **Left Column**: RN black hole with $Q/M = 0.9$, and the hot spot is situated at $r = r_{\text{msco}}$. This image showcases the primary and secondary lensed image tracks positioned outside the critical curve, arising from the $n = 0^>$ and $1^>$ light rays emitted by the hot spot, respectively. **Middle Column**: RN singularity with $Q/M = 1.05$, and the hot spot is situated at $r = r_{\text{msco}}^+$. The image reveals two image tracks located outside the critical curve, akin to the black hole case. Owing to the reflection of light rays entering the photon sphere, additional tracks emerge within the critical curve. **Right Column**: RN singularity with $Q/M = 1.1$, and the hot spot is situated at $r = r_{\text{msco}}^+$. This image displays finite image tracks due to the absence of a photon sphere. Moreover, the two tracks of $2^<$ and $2^>$ merge together.

FIG. 3 reveals the time integrated images for hot spots orbiting around a RN black hole at $r = r_{\text{msco}}$ and RN naked singularities at $r = r_{\text{msco}}^+$. The upper and lower panels show images observed at inclination angles of $\theta_o = 80^\circ$ and 50° , respectively. These images manifest several image tracks revealing the orbit of hot spots. To comprehend the origin of these tracks, we use the integer n to

indicate the number of times light rays intersect the equatorial plane. Furthermore, in the presence of a photon sphere in cases of the RN black hole with $Q/M = 0.9$ and the RN naked singularity with $Q/M = 1.05$, image tracks are separated by the critical curve, shaped by light rays with the critical impact parameter b_c . In the absence of a photon sphere ($Q/M = 1.1$), the deflection angle reaches a maximum value b_m as the impact parameter b varies. We therefore introduce superscripts $>$ and $<$ to distinguish light rays with $b > b_c$ (b_m) and $b < b_c$ (b_m), respectively.

The left column of FIG. 3 displays time integrated images of a hot spot orbiting an RN black hole with $Q/M = 0.9$ at $r = r_{\text{msco}}$. These images reveal a central shadow surrounded by a critical curve. For an observer's inclination angle of $\theta_o = 80^\circ$, the primary image ($n = 0^>$) exhibits a closed, semicircular track. Its upper and lower segments correspond to the hot spot behind and in front of the black hole, respectively. In contrast, the secondary image with $n = 1^>$ follows a smaller and fainter track. Moreover, images of higher order have significantly reduced luminosity and adhere closely to the critical curve. Additionally, these images exhibit a distinctive brightness asymmetry due to Doppler effects.

The image obtained at an observation inclination of $\theta_o = 50^\circ$ resembles the one at $\theta_o = 80^\circ$, but with a lower level of brightness asymmetry observed at the lower inclination. Furthermore, the image tracks are more circular at the lower inclination.

The middle column of FIG. 3 shows the time integrated image of a hot spot orbiting the RN singularity with $Q/M = 1.05$ at $r = r_{\text{msco}}^+$. There are two tracks outside the critical curve, resembling the scenario for the black hole at both observation inclinations of $\theta_o = 50^\circ$ and 80° . In contrast, four distinct tracks ($n = 0^<, 1^<, 2^<$ and $3^<$) appear within the critical curve, generated by light rays refracted around the naked singularity. Similarly, as the order n increases, the track becomes progressively more circular, exhibits significantly reduced luminosity, and closely follows the critical curve.

Unlike the previous cases, the absence of a photon sphere in the RN singularity with $Q/M = 1.1$ results in no critical curve within the time-integrated images for a hot spot orbiting at $r = r_{\text{msco}}^+$ (FIG. 3, right column). Instead, six distinct tracks are visible, denoted as $n = 0^<, 1^<, 2^<, 2^>, 1^>$ and $0^>$. Notably, the $2^<$ and $2^>$ tracks appear incomplete and converge when observed at $\theta_o = 80^\circ$, where their deflection angles $\alpha(b)$ reach their maximum. This merging behavior persists at an inclination angle of $\theta_o = 50^\circ$, although both $2^<$ and $2^>$ tracks seem complete in this case.

FIG. 4 depicts integrated images of RN singularities with $Q/M = 1.05$ and $Q/M = 1.1$, where the hot spots are orbiting at $r = 1.11M$ and $1.22M$, respectively. Due to their close proximity to the center, the light rays experience a significant gravitational influence, leading to the overlapping

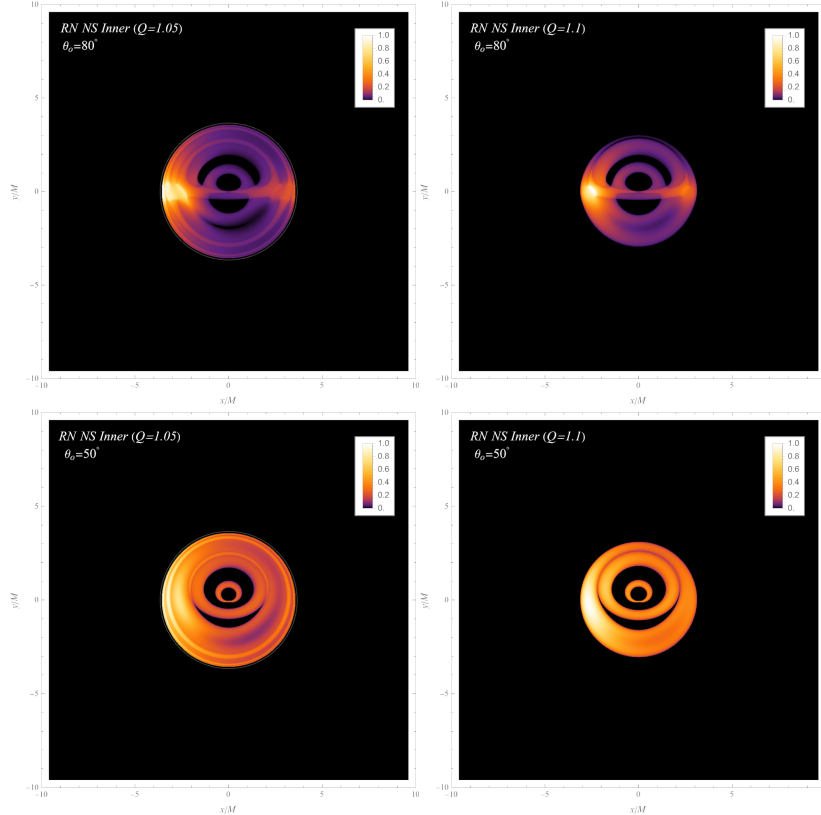


FIG. 4. Time integrated images depicting a full orbit of the hot spot positioned near $r = r^*$ in the RN singularity with $Q/M = 1.05$ (**Left Column**) and 1.1 (**Right Column**). These images are obtained from an observational inclination angle of $\theta_o = 80^\circ$ (**Upper Row**) and $\theta_o = 50^\circ$ (**Lower Row**). As a result of the reduced orbit radius, the resulting images are displayed in a smaller field of view. The tracks in the images appear overlapped and are challenging to distinguish.

of final image tracks, making them challenging to differentiate. For $Q/M = 1.05$, the orbit of the hot spot lies within the photon sphere, resulting in images bounded by the critical curve. Besides, higher-order images are dimly discerned near the critical curve, overlapped with the primary image. Conversely, for $Q/M = 1.1$, finite image tracks are observable, due to the absence of a photon sphere.

B. Temporal Fluxes and Centroids

To achieve a more profound comprehension of the alterations in integrated images, this part studies the temporal magnitudes m_k and centroids c_k observed at an inclination angle of $\theta_o = 80^\circ$ for each cases. FIGS. 5 and 6 highlight two significant peak in the temporal magnitude for each cases, labeled as ① and ②. Additionally, corresponding snapshot images at these specific moments

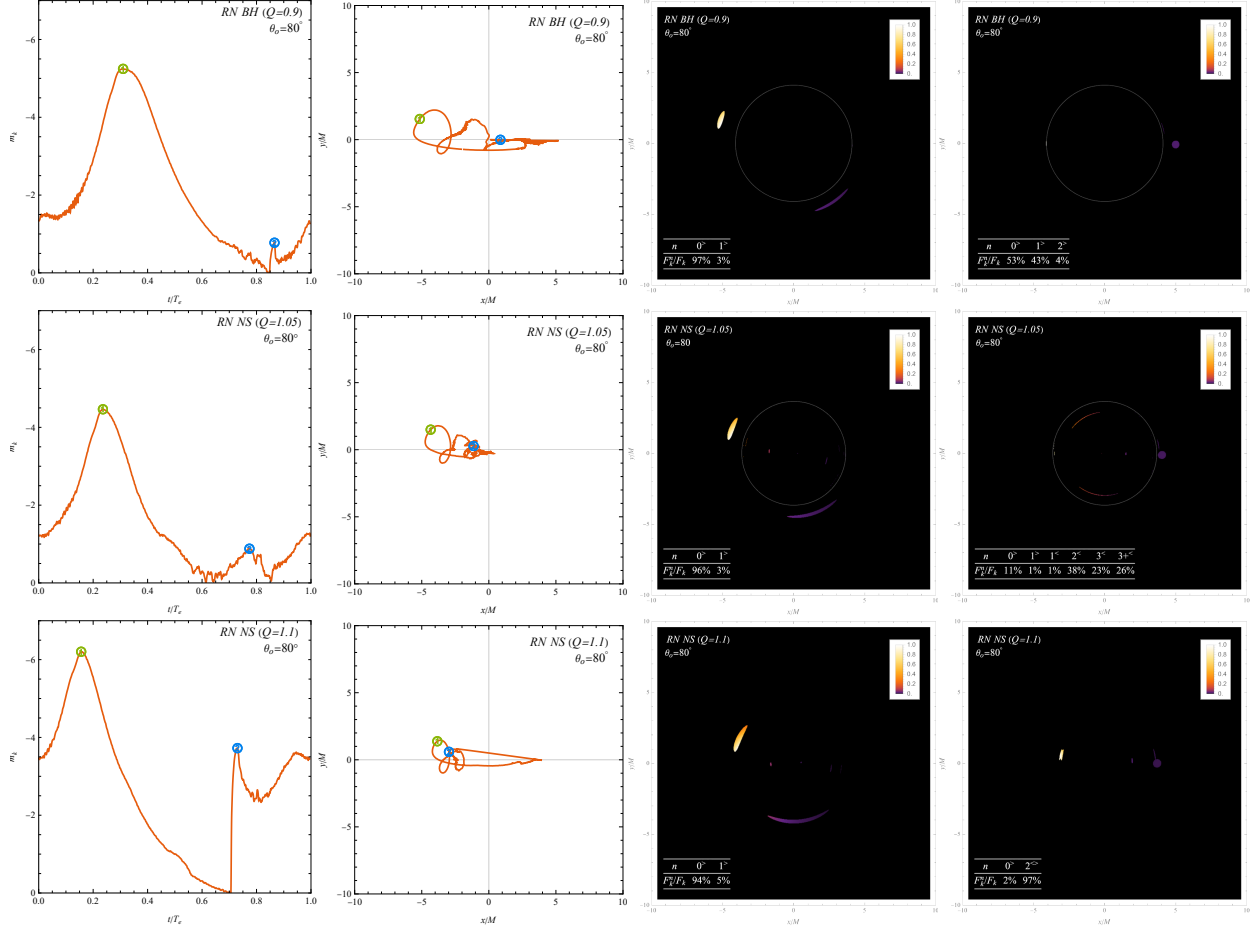


FIG. 5. Temporal magnitudes m_k (**First Column**) and centroids c_k (**Second Column**) as a function of t/T_e for cases $Q/M = 0.9$ with the orbit at r_{msco} (**Top Row**), $Q/M = 1.05$ (**Middle Row**) and $Q/M = 1.1$ with the orbit at r_{msco}^+ (**Bottom Row**). The inclination is $\theta_o = 80^\circ$. The highest and second-highest peaks of the temporal magnitude are indicated by ① and ②, respectively. The centroids of the flux at these peaks are identified with corresponding numbers. The snapshots for each cases, when the temporal magnitude reaches its highest peak and second-highest peak are presented in the third and fourth column, respectively. The contribution from the n^{th} -order image to the total flux is quantified by F_k^n/F_k , where F_k^n represents the temporal flux of the n^{th} -order image at $t = t_k$.

are provided for further examination.

FIG. 5 presents the results for three cases: the hot spot orbiting the RN black hole with $Q/M = 0.9$ at r_{msco} (top row), the hot spot orbiting the RN singularity with $Q/M = 1.05$ at r_{msco} (middle row), and the hot spot orbiting the RN singularity with $Q/M = 1.1$ at r_{msco}^+ (bottom row). In all cases, the primary image ($n = 0^\circ$) generated by the hot spot close to the leftmost portion of its orbit dominates the flux at the highest peak (as shown in third column). This aligns with our expectations based on the Doppler effect, as the hot spot approaching the observer on the left

side experiences a blue shift, leading to a noticeable increase in the observed flux.

Conversely, as the hot spot moves away from the observer, the primary image undergoes a phase of diminished flux, reducing its dominant contribution and allowing higher-order images to generate localized flux peaks. Notably, the secondary peak in each scenario reveals distinct contributors:

- In the $Q/M = 0.9$ case, the $n = 1^>$ image becomes a significant contributor to the total flux, leading to the secondary peak.
- In the $Q/M = 1.05$ case, the $n = 2^<$, $n = 3^<$ and higher-order images within critical curve collectively contribute to the secondary peak.
- In the $Q/M = 1.1$ case, the absence of a critical curve allows the $n = 2^<$ and $2^>$ images to emerge as dominant contributors at the secondary peak.

These distinct contributions to the secondary peak in each cases provide valuable features for differentiating between them.

The corresponding centroids are presented in the second column of FIG. 5. When the primary image exhibits relative dominance, the temporal centroid coincides with the primary image's center. Doppler-induced flux reduction in the primary image, coupled with the presence of higher-order images, can substantially displace the centroid from the center of the primary image's orbit, resulting in the observed intricate trajectory in the vicinity of the center. In the case of $Q/M = 1.05$, the presence of inner images further accentuates this intricacy of the centroid. Additionally, for $Q/M = 1.1$, the finite number of higher-order images leads to a smoother centroid.

FIG. 6 shows the results for two cases: the hot spots orbiting the RN black hole with $Q/M = 1.05$ (top row) and $Q/M = 1.1$ (bottom row) at $r = 1.11M$ and $1.22M$, respectively. Due to the small radius of the orbit, the hot spot appears proximate to the observer-singularity line. Notably, the structural symmetry facilitates the formation of a circular ring in the snapshot image. Furthermore, the high imaging symmetry contributes to a centroid position situated closer to the center.

In the end, we present the temporal magnitudes and centroids for an inclination angle of $\theta_o = 50^\circ$ in FIG. 7. In contrast to the inclination of $\theta_o = 80^\circ$, the temporal magnitudes at $\theta_o = 50^\circ$ exhibit a single peak. This difference arises from the reduced influence of the Doppler effect at the lower inclination angle. As a consequence, the flux becomes less frequency-dependent, allowing the primary image to dominate the total flux for a larger portion of the observation period. This, in turn, minimizes the impact of higher-order images on the centroids, leading to a smoother and less intricate trajectory.

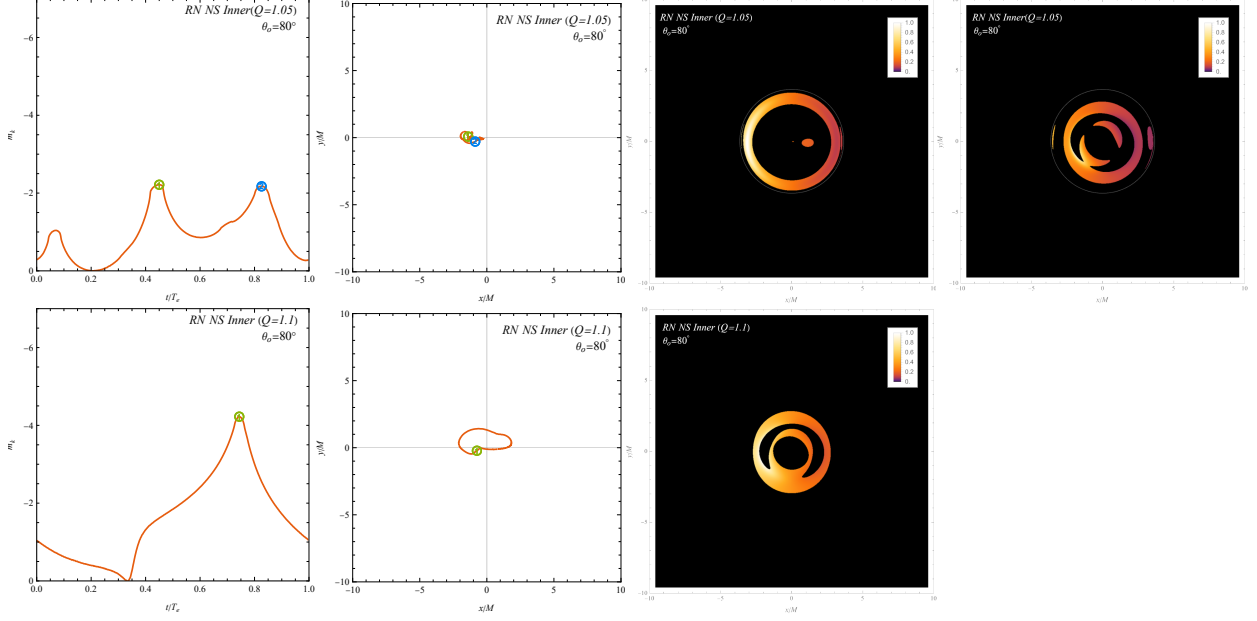


FIG. 6. Temporal magnitudes m_k (**First Column**) and centroids c_k (**Second Column**) as a function of t/T_e for cases $Q/M = 1.05$ (**Top Row**) and $Q/M = 1.1$ with the orbit near r^* (**Bottom Row**). The inclination is $\theta_o = 80^\circ$ as well. The highest and second-highest peaks of the temporal magnitude are indicated by ① and ②, respectively. The centroids of the flux at these peaks are identified with corresponding numbers. We also provide snapshots for the each cases, when the temporal magnitude reaches its highest peak (**Third Column**) and second-highest peak (**Fourth Column**). Note that only a single peak appears in the case of $Q/M = 1.1$.

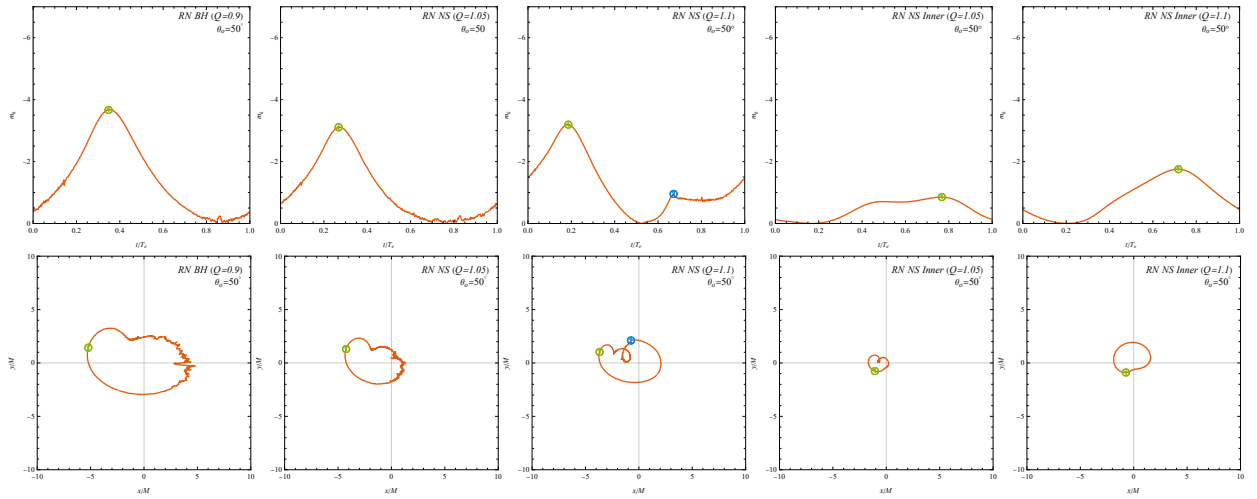


FIG. 7. Temporal magnitudes m_k (**Upper Row**) and centroids c_k (**Lower Row**) as a function of t/T_e for each cases. The inclination is $\theta_o = 50^\circ$.

V. CONCLUSIONS

This study investigates the observational signatures of RN black holes and singularities, focusing on the hot spots orbiting celestial bodies. Interestingly, the presence or absence of a photon sphere, which significantly impacts the observed features of the orbiting hot spots, surrounding a RN singularity depends on the charge parameter Q/M . To disentangle the diverse manifestations arising from different scenarios within RN spacetime, we compare the observational signatures of RN black holes, RN singularities with a photon sphere, and RN singularities without photon spheres. The main discrepancy is expected to be more pronounced at an observational inclination angle of $\theta_o = 80^\circ$, and we summarize these differences as follows:

- For the RN black hole case, the observed features closely resemble those of Schwarzschild black holes: two distinct lensing image tracks emerge in time-integrated images capturing a complete hot spot orbit.
- In contrast, for the RN naked singularity with a photon sphere, images outside the critical curve mirror those of black holes. However, unlike black holes, RN naked singularities can exhibit additional images within the critical curve, leading to a distinct second peak in the magnitude profiles.
- Intriguingly, the RN naked singularity without photon spheres display a finite number of tracks in the time-integrated image. Notably, incomplete and converging tracks appear. This merging and decomposition of tracks results in a rapid rise and fall of magnitudes, forming a pronounced second peak.

The analysis of these image characteristics serves as a powerful aid in distinguishing between RN black holes and singularities, and also contributes to exploring the nature of naked singularities and further assessing their potential as alternatives to black holes. With the advent of the next-generation Very Long Baseline Interferometry (VLBI), the ability to observe finer features is significantly enhanced. This will undoubtedly open up a wider range of potential avenues for detecting the aforementioned characteristics.

ACKNOWLEDGMENTS

We are grateful to Guangzhou Guo and Xin Jiang for useful discussions and valuable comments. This work is supported in part by NSFC (Grant No. 12105191, 11947225 and 11875196).

-
- [1] Kazunori Akiyama et al. First M87 Event Horizon Telescope Results. I. The Shadow of the Supermassive Black Hole. *Astrophys. J. Lett.*, 875:L1, 2019. [arXiv:1906.11238](#), [doi:10.3847/2041-8213/ab0ec7](#).
[I](#)
 - [2] Kazunori Akiyama et al. First M87 Event Horizon Telescope Results. II. Array and Instrumentation. *Astrophys. J. Lett.*, 875(1):L2, 2019. [arXiv:1906.11239](#), [doi:10.3847/2041-8213/ab0c96](#).
 - [3] Kazunori Akiyama et al. First M87 Event Horizon Telescope Results. III. Data Processing and Calibration. *Astrophys. J. Lett.*, 875(1):L3, 2019. [arXiv:1906.11240](#), [doi:10.3847/2041-8213/ab0c57](#).
 - [4] Kazunori Akiyama et al. First M87 Event Horizon Telescope Results. IV. Imaging the Central Supermassive Black Hole. *Astrophys. J. Lett.*, 875(1):L4, 2019. [arXiv:1906.11241](#), [doi:10.3847/2041-8213/ab0e85](#).
 - [5] Kazunori Akiyama et al. First M87 Event Horizon Telescope Results. V. Physical Origin of the Asymmetric Ring. *Astrophys. J. Lett.*, 875(1):L5, 2019. [arXiv:1906.11242](#), [doi:10.3847/2041-8213/ab0f43](#).
 - [6] Kazunori Akiyama et al. First M87 Event Horizon Telescope Results. VI. The Shadow and Mass of the Central Black Hole. *Astrophys. J. Lett.*, 875(1):L6, 2019. [arXiv:1906.11243](#), [doi:10.3847/2041-8213/ab1141](#).
 - [7] Kazunori Akiyama et al. First M87 Event Horizon Telescope Results. VII. Polarization of the Ring. *Astrophys. J. Lett.*, 910(1):L12, 2021. [arXiv:2105.01169](#), [doi:10.3847/2041-8213/abe71d](#).
 - [8] Kazunori Akiyama et al. First M87 Event Horizon Telescope Results. VIII. Magnetic Field Structure near The Event Horizon. *Astrophys. J. Lett.*, 910(1):L13, 2021. [arXiv:2105.01173](#), [doi:10.3847/2041-8213/abe4de](#).
 - [9] Kazunori Akiyama et al. First Sagittarius A* Event Horizon Telescope Results. I. The Shadow of the Supermassive Black Hole in the Center of the Milky Way. *Astrophys. J. Lett.*, 930(2):L12, 2022. [doi:10.3847/2041-8213/ac6674](#).
 - [10] Kazunori Akiyama et al. First Sagittarius A* Event Horizon Telescope Results. II. EHT and Multiwavelength Observations, Data Processing, and Calibration. *Astrophys. J. Lett.*, 930(2):L13, 2022. [doi:10.3847/2041-8213/ac6675](#).
 - [11] Kazunori Akiyama et al. First Sagittarius A* Event Horizon Telescope Results. III. Imaging of the Galactic Center Supermassive Black Hole. *Astrophys. J. Lett.*, 930(2):L14, 2022. [doi:10.3847/2041-8213/ac6429](#).

- [12] Kazunori Akiyama et al. First Sagittarius A* Event Horizon Telescope Results. IV. Variability, Morphology, and Black Hole Mass. *Astrophys. J. Lett.*, 930(2):L15, 2022. doi:10.3847/2041-8213/ac6736.
- [13] Kazunori Akiyama et al. First Sagittarius A* Event Horizon Telescope Results. V. Testing Astrophysical Models of the Galactic Center Black Hole. *Astrophys. J. Lett.*, 930(2):L16, 2022. doi:10.3847/2041-8213/ac6672.
- [14] Kazunori Akiyama et al. First Sagittarius A* Event Horizon Telescope Results. VI. Testing the Black Hole Metric. *Astrophys. J. Lett.*, 930(2):L17, 2022. doi:10.3847/2041-8213/ac6756. I
- [15] Clifford M. Will. The Confrontation between General Relativity and Experiment. *Living Rev. Rel.*, 17:4, 2014. arXiv:1403.7377, doi:10.12942/lrr-2014-4. I
- [16] Roy P. Kerr. Gravitational field of a spinning mass as an example of algebraically special metrics. *Phys. Rev. Lett.*, 11:237–238, 1963. doi:10.1103/PhysRevLett.11.237. I
- [17] Roger Penrose. Gravitational collapse and space-time singularities. *Phys. Rev. Lett.*, 14:57–59, Jan 1965. URL: <https://link.aps.org/doi/10.1103/PhysRevLett.14.57>, doi:10.1103/PhysRevLett.14.57. I
- [18] J. L. Synge. The Escape of Photons from Gravitationally Intense Stars. *Mon. Not. Roy. Astron. Soc.*, 131(3):463–466, 1966. doi:10.1093/mnras/131.3.463. I
- [19] James M. Bardeen, William H. Press, and Saul A Teukolsky. Rotating black holes: Locally nonrotating frames, energy extraction, and scalar synchrotron radiation. *Astrophys. J.*, 178:347, 1972. doi:10.1086/151796.
- [20] J. M. Bardeen. Timelike and null geodesics in the Kerr metric. In *Les Houches Summer School of Theoretical Physics: Black Holes*, 1973.
- [21] K. S. Virbhadra and George F. R. Ellis. Schwarzschild black hole lensing. *Phys. Rev. D*, 62:084003, 2000. arXiv:astro-ph/9904193, doi:10.1103/PhysRevD.62.084003.
- [22] Clarissa-Marie Claudel, K. S. Virbhadra, and G. F. R. Ellis. The Geometry of photon surfaces. *J. Math. Phys.*, 42:818–838, 2001. arXiv:gr-qc/0005050, doi:10.1063/1.1308507.
- [23] K. S. Virbhadra. Relativistic images of Schwarzschild black hole lensing. *Phys. Rev. D*, 79:083004, 2009. arXiv:0810.2109, doi:10.1103/PhysRevD.79.083004.
- [24] Valerio Bozza. Gravitational Lensing by Black Holes. *Gen. Rel. Grav.*, 42:2269–2300, 2010. arXiv:0911.2187, doi:10.1007/s10714-010-0988-2.
- [25] K. S. Virbhadra. Distortions of images of Schwarzschild lensing. *Phys. Rev. D*, 106(6):064038, 2022. arXiv:2204.01879, doi:10.1103/PhysRevD.106.064038. I
- [26] Fabian Schmidt. Weak Lensing Probes of Modified Gravity. *Phys. Rev. D*, 78:043002, 2008. arXiv:0805.4812, doi:10.1103/PhysRevD.78.043002. I
- [27] Jacek Guzik, Bhuvnesh Jain, and Masahiro Takada. Tests of Gravity from Imaging and Spectroscopic Surveys. *Phys. Rev. D*, 81:023503, 2010. arXiv:0906.2221, doi:10.1103/PhysRevD.81.023503.
- [28] Kai Liao, Zhengxiang Li, Shuo Cao, Marek Biesiada, Xiaogang Zheng, and Zong-Hong Zhu. The

- Distance Duality Relation From Strong Gravitational Lensing. *Astrophys. J.*, 822(2):74, 2016. [arXiv:1511.01318](#), [doi:10.3847/0004-637X/822/2/74](#).
- [29] Prieslei Goulart. Phantom wormholes in Einstein–Maxwell-dilaton theory. *Class. Quant. Grav.*, 35(2):025012, 2018. [arXiv:1708.00935](#), [doi:10.1088/1361-6382/aa9dfc](#).
- [30] J. R. Nascimento, A. Yu. Petrov, P. J. Porfirio, and A. R. Soares. Gravitational lensing in black-bounce spacetimes. *Phys. Rev. D*, 102(4):044021, 2020. [arXiv:2005.13096](#), [doi:10.1103/PhysRevD.102.044021](#).
- [31] Shafqat Ul Islam, Jitendra Kumar, and Sushant G. Ghosh. Strong gravitational lensing by rotating Simpson-Visser black holes. *JCAP*, 10:013, 2021. [arXiv:2104.00696](#), [doi:10.1088/1475-7516/2021/10/013](#).
- [32] Naoki Tsukamoto. Gravitational lensing by two photon spheres in a black-bounce spacetime in strong deflection limits. *Phys. Rev. D*, 104(6):064022, 2021. [arXiv:2105.14336](#), [doi:10.1103/PhysRevD.104.064022](#).
- [33] Haroldo C. D. Lima Junior, Jian-Zhi Yang, Luís C. B. Crispino, Pedro V. P. Cunha, and Carlos A. R. Herdeiro. Einstein-Maxwell-dilaton neutral black holes in strong magnetic fields: Topological charge, shadows, and lensing. *Phys. Rev. D*, 105(6):064070, 2022. [arXiv:2112.10802](#), [doi:10.1103/PhysRevD.105.064070](#).
- [34] Gonzalo J. Olmo, Diego Rubiera-Garcia, and Diego Sáez-Chillón Gómez. New light rings from multiple critical curves as observational signatures of black hole mimickers. *Phys. Lett. B*, 829:137045, 2022. [arXiv:2110.10002](#), [doi:10.1016/j.physletb.2022.137045](#).
- [35] Saptaswa Ghosh and Arpan Bhattacharyya. Analytical study of gravitational lensing in Kerr-Newman black-bounce spacetime. *JCAP*, 11:006, 2022. [arXiv:2206.09954](#), [doi:10.1088/1475-7516/2022/11/006](#). I
- [36] D. Ayzenberg et al. Fundamental Physics Opportunities with the Next-Generation Event Horizon Telescope. 12 2023. [arXiv:2312.02130](#). I
- [37] Stuart L. Shapiro and Saul A. Teukolsky. Formation of naked singularities: The violation of cosmic censorship. *Phys. Rev. Lett.*, 66:994–997, 1991. [doi:10.1103/PhysRevLett.66.994](#). I
- [38] P. S. Joshi and I. H. Dwivedi. Naked singularities in spherically symmetric inhomogeneous Tolman-Bondi dust cloud collapse. *Phys. Rev. D*, 47:5357–5369, 1993. [arXiv:gr-qc/9303037](#), [doi:10.1103/PhysRevD.47.5357](#).
- [39] Tomohiro Harada, Hideo Iguchi, and Ken-ichi Nakao. Naked singularity formation in the collapse of a spherical cloud of counter rotating particles. *Phys. Rev. D*, 58:041502, 1998. [arXiv:gr-qc/9805071](#), [doi:10.1103/PhysRevD.58.041502](#).
- [40] Pankaj S. Joshi, Naresh Dadhich, and Roy Maartens. Why do naked singularities form in gravitational collapse? *Phys. Rev. D*, 65:101501, 2002. [arXiv:gr-qc/0109051](#), [doi:10.1103/PhysRevD.65.101501](#).
- [41] Rituparno Goswami and Pankaj S Joshi. Spherical gravitational collapse in N-dimensions. *Phys. Rev. D*, 76:084026, 2007. [arXiv:gr-qc/0608136](#), [doi:10.1103/PhysRevD.76.084026](#).

- [42] Narayan Banerjee and Soumya Chakrabarti. Self-similar scalar field collapse. *Phys. Rev. D*, 95(2):024015, 2017. [arXiv:1701.04235](#), [doi:10.1103/PhysRevD.95.024015](#).
- [43] Kaushik Bhattacharya, Dipanjan Dey, Arindam Mazumdar, and Tapobrata Sarkar. New class of naked singularities and their observational signatures. *Phys. Rev. D*, 101(4):043005, 2020. [arXiv:1709.03798](#), [doi:10.1103/PhysRevD.101.043005](#). I
- [44] K. S. Virbhadra and G. F. R. Ellis. Gravitational lensing by naked singularities. *Phys. Rev. D*, 65:103004, 2002. [doi:10.1103/PhysRevD.65.103004](#). I
- [45] K. S. Virbhadra and C. R. Keeton. Time delay and magnification centroid due to gravitational lensing by black holes and naked singularities. *Phys. Rev. D*, 77:124014, 2008. [arXiv:0710.2333](#), [doi:10.1103/PhysRevD.77.124014](#).
- [46] Galin N. Gylchev and Stoytcho S. Yazadjiev. Gravitational Lensing by Rotating Naked Singularities. *Phys. Rev. D*, 78:083004, 2008. [arXiv:0806.3289](#), [doi:10.1103/PhysRevD.78.083004](#).
- [47] Satyabrata Sahu, Mandar Patil, D. Narasimha, and Pankaj S. Joshi. Can strong gravitational lensing distinguish naked singularities from black holes? *Phys. Rev. D*, 86:063010, 2012. [arXiv:1206.3077](#), [doi:10.1103/PhysRevD.86.063010](#).
- [48] Rajibul Shaikh, Pritam Banerjee, Suvankar Paul, and Tapobrata Sarkar. Analytical approach to strong gravitational lensing from ultracompact objects. *Phys. Rev. D*, 99(10):104040, 2019. [arXiv:1903.08211](#), [doi:10.1103/PhysRevD.99.104040](#). I
- [49] Suvankar Paul. Strong gravitational lensing by a strongly naked null singularity. *Phys. Rev. D*, 102(6):064045, 2020. [arXiv:2007.05509](#), [doi:10.1103/PhysRevD.102.064045](#).
- [50] V. I. Zhdanov and O. S. Stashko. Static spherically symmetric configurations with N nonlinear scalar fields: Global and asymptotic properties. *Phys. Rev. D*, 101(6):064064, 2020. [arXiv:1912.00470](#), [doi:10.1103/PhysRevD.101.064064](#).
- [51] O. S. Stashko, V. I. Zhdanov, and A. N. Alexandrov. Thin accretion discs around spherically symmetric configurations with nonlinear scalar fields. *Phys. Rev. D*, 104(10):104055, 2021. [arXiv:2107.05111](#), [doi:10.1103/PhysRevD.104.104055](#).
- [52] Oleksandr Stashko and Valery I. Zhdanov. Singularities in Static Spherically Symmetric Configurations of General Relativity with Strongly Nonlinear Scalar Fields. *Galaxies*, 9(4):72, 2021. [arXiv:2109.01931](#), [doi:10.3390/galaxies9040072](#).
- [53] Naoki Tsukamoto. Gravitational lensing by a photon sphere in a Reissner-Nordström naked singularity spacetime in strong deflection limits. *Phys. Rev. D*, 104(12):124016, 2021. [arXiv:2107.07146](#), [doi:10.1103/PhysRevD.104.124016](#).
- [54] Mingzhi Wang, Guanghai Guo, Pengfei Yan, Songbai Chen, and Jiliang Jing. The images of a rotating naked singularity with a complete photon sphere. 7 2023. [arXiv:2307.16748](#).
- [55] Yiqian Chen, Peng Wang, Houwen Wu, and Haitang Yang. Gravitational Lensing by Born-Infeld Naked Singularities. 5 2023. [arXiv:2305.17411](#). I, III, III
- [56] J. Dexter et al. Sgr A* near-infrared flares from reconnection events in a magnetically arrested

- disc. *Mon. Not. Roy. Astron. Soc.*, 497(4):4999–5007, 2020. [arXiv:2006.03657](#), [doi:10.1093/mnras/staa2288](#). I
- [57] Nicolas Scepi, Jason Dexter, and Mitchell C. Begelman. Sgr A* X-ray flares from non-thermal particle acceleration in a magnetically arrested disc. *Mon. Not. Roy. Astron. Soc.*, 511(3):3536–3547, 2022. [arXiv:2107.08056](#), [doi:10.1093/mnras/stac337](#).
- [58] I. El Mellah, B. Cerutti, B. Crinquand, and K. Parfrey. Spinning black holes magnetically connected to a Keplerian disk - Magnetosphere, reconnection sheet, particle acceleration, and coronal heating. *Astron. Astrophys.*, 663:A169, 2022. [arXiv:2112.03933](#), [doi:10.1051/0004-6361/202142847](#). I
- [59] G. Witzel et al. Rapid Variability of Sgr A* across the Electromagnetic Spectrum. *Astrophys. J.*, 917(2):73, 2021. [arXiv:2011.09582](#), [doi:10.3847/1538-4357/ac0891](#). I
- [60] Joseph M. Michail, Mark Wardle, Farhad Yusef-Zadeh, and Devaky Kunneriath. Multiwavelength Observations of Sgr A*. I. 2019 July 18. *Astrophys. J.*, 923(1):54, 2021. [arXiv:2107.09681](#), [doi:10.3847/1538-4357/ac2d2c](#).
- [61] R. Abuter et al. Constraining particle acceleration in Sgr A* with simultaneous GRAVITY, Spitzer, NuSTAR, and Chandra observations. *Astron. Astrophys.*, 654:A22, 2021. [arXiv:2107.01096](#), [doi:10.1051/0004-6361/202140981](#). I
- [62] Maciek Wielgus, Monika Moscibrodzka, Jesse Vos, Zachary Gelles, Ivan Marti-Vidal, Joseph Farah, Nicola Marchili, Ciriaco Goddi, and Hugo Messias. Orbital motion near Sagittarius A* - Constraints from polarimetric ALMA observations. *Astron. Astrophys.*, 665:L6, 2022. [arXiv:2209.09926](#), [doi:10.1051/0004-6361/202244493](#). I
- [63] N. Hamaus, T. Paumard, T. Muller, S. Gillessen, F. Eisenhauer, S. Trippe, and R. Genzel. Prospects for testing the nature of Sgr A*'s NIR flares on the basis of current VLT- and future VLTI-observations. *Astrophys. J.*, 692:902–916, 2009. [arXiv:0810.4947](#), [doi:10.1088/0004-637X/692/1/902](#). I, IV
- [64] Roberto Abuter, A Amorim, M Bauböck, JP Berger, H Bonnet, W Brandner, Y Clénet, V Coudé Du Foresto, PT de Zeeuw, C Deen, et al. Detection of orbital motions near the last stable circular orbit of the massive black hole sgra. *Astronomy & Astrophysics*, 618:L10, 2018.
- [65] João Luís Rosa, Paulo Garcia, Frédéric H. Vincent, and Vitor Cardoso. Observational signatures of hot spots orbiting horizonless objects. *Phys. Rev. D*, 106(4):044031, 2022. [arXiv:2205.11541](#), [doi:10.1103/PhysRevD.106.044031](#). IV
- [66] João Luís Rosa, Caio F. B. Macedo, and Diego Rubiera-Garcia. Imaging compact boson stars with hot spots and thin accretion disks. *Phys. Rev. D*, 108(4):044021, 2023. [arXiv:2303.17296](#), [doi:10.1103/PhysRevD.108.044021](#). IV
- [67] Hanna Liis Tamm and João Luís Rosa. Observational properties of hot-spots orbiting relativistic fluid spheres. 10 2023. [arXiv:2310.12681](#).
- [68] João Luís Rosa, Daniela S. J. Cordeiro, Caio F. B. Macedo, and Francisco S. N. Lobo. Observational imprints of gravastars from accretion disks and hot-spots. 1 2024. [arXiv:2401.07766](#). I
- [69] D. Pugliese, H. Quevedo, and R. Ruffini. Circular motion of neutral test particles in Reissner-Nordström

- spacetime. *Phys. Rev. D*, 83:024021, 2011. [arXiv:1012.5411](#), [doi:10.1103/PhysRevD.83.024021](#). I, II
- [70] D. Pugliese, H. Quevedo, and R. Ruffini. Motion of charged test particles in Reissner-Nordström spacetime. *Phys. Rev. D*, 83:104052, 2011. [arXiv:1103.1807](#), [doi:10.1103/PhysRevD.83.104052](#). II
- [71] Deyou Chen, Yiqian Chen, Peng Wang, Tianshu Wu, and Houwen Wu. Gravitational Lensing by Transparent Janis-Newman-Winicour Naked Singularities. 9 2023. [arXiv:2309.00905](#). III
- [72] Sascha Trippe, T. Paumard, T. Ott, S. Gillessen, F. Eisenhauer, F. Martins, and R. Genzel. A polarised infrared flare from Sagittarius A* and the signatures of orbiting plasma hotspots. *Mon. Not. Roy. Astron. Soc.*, 375:764–772, 2007. [arXiv:astro-ph/0611737](#), [doi:10.1111/j.1365-2966.2006.11338.x](#). IV
- [73] Avery E. Broderick and Abraham Loeb. Imaging optically-thin hot spots near the black hole horizon of sgr a* at radio and near-infrared wavelengths. *Mon. Not. Roy. Astron. Soc.*, 367:905–916, 2006. [arXiv:astro-ph/0509237](#), [doi:10.1111/j.1365-2966.2006.10152.x](#). IV
- [74] Yiqian Chen, Peng Wang, and Haitang Yang. Observations of Orbiting Hot Spots around Naked Singularities. 9 2023. [arXiv:2309.04157](#). IV